



POLITECNICO
MILANO 1863

DIPARTIMENTO DI MECCANICA



An Acoustic Emission-Based Approach To Structural Health Monitoring Of Pre-Stressed Concrete Railway Sleepers

M Carboni, A Collina and E Zappa

This is a post-peer-review, pre-copyedit version of an article published in Insight - Non-Destructive Testing & Condition Monitoring (ISSN: 1354-2575). The final authenticated version is available online at: <http://dx.doi.org/10.1784/insi.2020.62.5.280>

This content is provided under [CC BY-NC 4.0](https://creativecommons.org/licenses/by-nc/4.0/) license



An Acoustic Emission-based Approach to Structural Health Monitoring of Railway Pre-stressed Concrete Sleepers[♣]

Michele CARBONI^{1*}, Andrea COLLINA¹, Emanuele ZAPPA¹

¹*Politecnico di Milano, Dept. Mechanical Engineering, Via La Masa 1, 20156 Milano, Italy*

Abstract

Railway sleepers represent an essential element of the track, indeed their structural integrity is strictly related to important technical and safety issues. Today, periodical visual inspections are the only method applied to check the status of sleepers, and besides limited to their visible surface, whereas an early detection of service cracks in their whole volume would provide great advantage in terms of maintenance and management. Aim of the paper is to propose an acoustic emission based structural health monitoring approach able to detect the initiation and propagation of cracks in in-service prestressed concrete sleepers. The investigation is carried out in the lab comparing the results obtained, by acoustic emission and by digital image correlation, subjecting prestressed concrete sleepers, taken from production, to both static and cyclic loads. The main points dealt with, in the paper, include the sensitivity of acoustic emission to detect damage development and the signal processing needed for defining effective damage indexes. Given the encouraging results, the paper is the first step for developing an affordable monitoring system, to be embedded into sleepers, able to be part of a complete track monitoring system.

Keywords: structural health monitoring, railway pre-stressed concrete sleepers, acoustic emission, digital image correlation, artificial neural networks

[♣] This is an extended version of the paper presented at the International Symposium on Structural Health Monitoring and Nondestructive Testing, 4-5 October 2018, Saarbruecken, Germany.

* Corresponding Author: Tel.: +39-02-23998253, Fax: +39-02-23998202, e-mail: michele.carboni@polimi.it (M. Carboni).

1. INTRODUCTION

Railway sleepers are that part of the track that transfers train axle loads from the rails to the ballast, while keeping both their correct gauge and their inclination at the correct values. In order to guarantee rail operation safety, they are required to withstand the direct mechanical interactions with axle loads of the trains in transit and the effect of the long-term degradation of ballast and subgrade occurring during service [1]. Wood sleepers (termed also as timber sleepers), concrete sleepers and, to a limited extent, steel sleepers are generally adopted along the main railway networks [2]. In addition, the use of polymeric or reinforced polymeric sleepers is now being studied and the first products are available for specific applications (fixed and movable bridges, switches). Today, pre-stressed concrete sleepers (Fig. 1) are the most common type applied in railway networks, from 60% to 80% of the total, depending on the network [2]. They are characterized by several advantages, such as [1]:

- their mass, in the range of 200-350 kg, is exploited to improve stability of continuous welded rail tracks against buckling. The mass is also particularly important for the dynamical behaviour of the track at high speed and it was firstly introduced in the Tokaido line in Japan, on purpose, in the 60s;
- longer expected service life (more than 50 years) with respect to timber sleepers;
- higher design flexibility in terms of shape and load carrying capabilities. As for the former, cavities and passages for cables can be easily obtained in the casting process;
- simplicity in manufacturing;
- high availability of the material (concrete and steel) with respect to wood essence, which starts to show difficulties on procurement of good quality material.

Nevertheless, they show some drawbacks, as well:

- compared to timber sleepers, they have a higher stiffness of the contact surface with ballast, leading to a higher rate of ballast crushing. This drawback is mitigated, when required, by the adoption of under-sleeper pads [3];
- compared to timber sleepers, they show a higher sensitivity to damage due to the work of tamping machines;

- failure can be originated by the initiation of cracks due to several different causes, as discussed below. This is the main object of the monitoring system proposed in the present research.

Pre-stressed concrete monoblock sleepers can be considered, from a structural point of view, as unidirectional composite beams subjected to bending, with a distributed elastic reaction coming from the ballast underneath, and a couple of vertical and lateral loads coming from wheel-rail interactions. In particular, the matrix of the composite beam consists of concrete, which is a ceramic (brittle) granular and aggregated material characterized by failure planes oriented perpendicularly to the axis of the acting loads. To achieve the needed strength, such a matrix is pre-stressed by means of unidirectional “fibers” represented by metallic reinforcing bars or tendons (cables), from four to eight equally distributed above and below the neutral axis of the section, in order to withstand positive and negative longitudinal stresses due to the applied bending moments. Manufacturing is realized by casting, during which the reinforcing tendons are inserted in a pre-stressed tensile condition. When the concrete starts to solidify, the reinforcing tendons are released to generate the compressive stress state into the concrete matrix. In most cases, tendons are bonded to the concrete, but there are also configurations where they are non-adherent.

The most critical regions of concrete sleepers are the mid-span region and the rail-seat one, where fastenings with rails are located. Failures are related, along with the mechanical properties and behaviour of the adopted materials and their treatment, to service loads. In particular, the dominating load condition is typically represented by bending moments able to cause damage accumulation and progressive cracking of the sleeper with train transit. This situation is worsened if such bending moments become unexpectedly high due to a non-uniform distribution of ballast under the sleeper [1] and/or in the case of high loaded travelling axles [4]. Moreover, impact loads, due to a wheel flat or to poorly maintained rail joints, can be occasionally observed ([2], [5]-[6]): such loads can initiate cracks, subsequently propagated by the repeated loads due to travelling trains. Finally, chemical aggression can occur during service, as well: the most typical is the Delayed Ettringite Formation, happening in presence of peculiar environmental conditions.

Whatever it is the cause, initiation and propagation of cracks are more complex with respect to the case of an isotropic and homogeneous material, because the partialisation of the section is counteracted by the effect of the prestressed tendons. In particular, crack initiation is typically related to the overcome of the

pretension effect at the tensioned side of the bent section, while the final failure of the section is mostly related to the compression stress at the opposite side, with respect to the neutral axis, of the bent section. The situation is worsened by the brittle mechanical behaviour of concrete, which presents a failure mode characterized [7] by an unstable and instantaneous release of fracture energy without the onset of plasticity and the related collaboration of the ligament to the strength of the damaged section. Moreover, and contrarily to ductile materials, a brittle one provides no warning about an approaching failure.

Since sleepers are safety critical elements, several standards are available in the European framework. The most important is the EN 13230 [8] (Railway applications – Track – Concrete sleepers and bearers), which defines the experimental tests to be carried out on finished products for homologation. Tests are carried out suitably loading full-scale specimens, i.e. real sleepers directly taken from production, with specified loading condition for generating bending moments at mid-span and rail seat sections. Three different kinds of tests are described in [8]: i) static bending test; ii) dynamic bending test, in which a dynamic load condition is applied in order to simulate impact load and cyclic loads; iii) (optional) fatigue bending test, in which a constant amplitude fatigue loading condition is provided.

Today, the methodologies for in-service inspection of concrete sleepers, each characterized by peculiar advantages and drawbacks, belong to the frame of Non-Destructive Testing (NDT) and mainly consist [9] in on-site visual inspections by a maintenance crew or by automated cameras located on board of diagnostic trains. Attempts have been done [10] to use a simplified modal data analysis carried out on site. For all these methods, the policy follows the protocol of the so-called “inspection interval based maintenance” according to a “Damage Tolerant” paradigm [11]. Nevertheless, a limited number of in-service failures still occurs. If specific causes exist, e.g. peculiar combinations of site conditions and high axle loads, the percentage of cracked sleepers can be rather large, ranging from 5% up to 15% or even more [4]. A novel approach to the problem might then be based on shifting from NDT to Structural Health Monitoring (SHM) techniques, which draw their origins on the need of preventing catastrophic failures in different fields. The idea is to detect and monitor, on either real-time or on-demand, developing damages before their evolution in structural collapse, thus to guarantee and improve the safety and reliability of different systems. Moreover, the application of SHM to the aerospace and civil fields has shown [12] the possibility

to reduce the cost of in-service maintenance by up to 30%, mainly because maintenance service interruption are no more periodically scheduled, but applied on purpose. Among the SHM methods under study for concrete structures, acoustic emission is one of the most widespread in the literature ([13]-[14]).

The present paper describes a feasibility analysis about the application of acoustic emission (AE) to the detection and monitoring of cracks in pre-stressed concrete sleepers. For the purpose of assessment, the obtained results are compared to other methods: 2D digital image correlation (2D DIC, [15]), here used to quantitatively define crack opening and often adopted for crack monitoring in concrete structures ([16]-[17]), and visual testing (VT). Encouraging results indicate the possibility to carry out more validating tests in order to get the engineering of a suitably affordable monitoring system for in-service applications. It is worth mentioning that the proposed approach enables to detect cracks also in the portion of the sleeper not visually accessible, i.e. the lower and the lateral surfaces, surrounded by ballast.

2. EXPERIMENTAL ACTIVITIES ON PRE-STRESSED CONCRETE SLEEPERS

In the frame of the present research, two experimental full-scale tests were carried out according to the relevant European standard for the homologation of railway pre-stressed concrete sleepers (EN 13230 [8]).

In particular, the two tests consisted in:

1. a three-point bending static test applied at the mid-span section of a RFI 230 sleeper;
2. a three-point bending dynamic test applied at the rail seat section of a RFI 260 sleeper.

Both the adopted full-scale specimens consisted in railway sleepers taken from production batches to be put in service along the Italian railway network. It is worth adding that, according to the Italian railway network operator (RFI), the nomenclature of sleepers consists in [18] a code of the type "RFI ####" where #### is the longitudinal length in centimetres. More details on both the experimental set-ups are reported in the following Sections.

2.1. Three-point bending static test of a RFI 230 sleeper

A RFI 230 type pre-stressed concrete sleeper was tested in the lab, at the mid-span section (Fig. 2a), by a three point bending static load according to [8]. In particular, a 300 kN servo-hydraulic actuator, controlled

in force, was employed. Two articulated supports were placed under the sleeper at the distance prescribed by the standard. In order to avoid crack initiation and propagation at supports, rubber pads, one for each support, were used; they provided a better load distribution at contact surfaces, as well. An articulated support and a rubber pad were also used at the application point of the load generated by the actuator. The applied time-load history (Fig. 2b) consisted in increasing the load, with a maximum rate of 120 kN/min, by sequential 5 kN increments interspersed by constant load time intervals lasting from 10 s to 5 min and up to the final failure of the sleeper.

Considering the application of SHM and NDT, AE was continuously acquired during the whole duration of the test, while, in order to get a feedback about the development of damage in the sleeper, VT and 2D DIC were carried out at the constant load time intervals of the load plan.

2.2. Dynamic test of a RFI 260 sleeper

In this case, a RFI 260 type pre-stressed concrete sleeper was tested in the lab, at the rail seat section (Fig. 2c), by a three point bending dynamic load according to [8]. In particular, a 1000 kN servo-hydraulic actuator, controlled in force, was employed. Suitable articulated supports and rubber pads were adopted, again, according to the standard. The applied time-load history (Fig. 2d) consisted in a sequence of fatigue block loads, each one applying 5000 fatigue cycles, characterized by the same minimum load level (50 kN) and a maximum load level increasing, from any block to the following one, by 20 kN. The test was carried out up to the final failure of the sleeper.

AE was, again, continuously acquired during the whole duration of the test, while VT and 2D DIC were carried out, at the end of each fatigue block load, applying a static load equal to 50 kN to the tested sleeper.

2.3. Structural health monitoring and non-destructive testing

AE activity was acquired by a Vallen Systeme AMSY-6 control unit with eight channels and by applying six sensors to both the tested sleepers (Fig. 3a and 3b): two at the ends and the other four closer to the region of interest, i.e. the region where cracks were supposed to initiate, on the lateral sides. The four closest

sensors were expected to be more sensitive than the farthest ones, but the two sensors at the ends were applied thinking to possible in-field applications. Sensors were coupled to concrete by means of a silicon couplant, while their slippage and detaching were avoided by taper. The measurement chain, for each channel, was constituted by one AE piezoelectric sensor (Vallen VS150-M with resonance frequency equal to 150 kHz) linked to a preamplifier (AEP4 34 dB) leading to the ASIP-2, a dual channels AE-signal processor card. Each AE event was recorded in terms of its full waveform, and without any filtering, in order to get the highest flexibility during the post-processing and the analysis of the phenomenon. The sample frequency was set to 10 MHz, while the HSU-Nielsen pencil response [19] allowed the calibration of the sound velocity in the tested concrete sleepers (3320 m/s). Finally, a 1D linear localization process was activated between the two sensors located at the ends and for each pair of sensors located close to the region of interest and lying on the same lateral side of the tested sleeper.

VT was applied by means of digital microscope Dino-Lite AM4113/AD4113 connected to an external PC. It was thus possible to record images with a 20x magnification and a resolution of 0.01 mm.

During the static test, 2D DIC images were recorded by means of a GX3300 digital camera equipped with a Zeiss Makro Planar lens of 50 mm optical length. The camera was mounted on a tripod in the front of the tested sleeper, to face the area where cracks were most likely to appear, and was connected to an external PC controlling the camera itself by means of a custom software developed in National Instruments LabVIEW environment. Since good lighting conditions were required, two LED lamps were used. A camera calibration procedure was carried out in order to compensate for perspective distortion and to define the conversion scale from pixel to millimetres (0.083 mm/pixel). The region of interest was speckled (Fig. 3c) by an airbrush, a compressor and black opaque paint. To create a controlled speckle size and distribution, a chemically machined steel plate was used as a stencil. The feature pattern of the obtained speckle is characterized by an average diameter of 3-5 pixel and a coverage factor of 40%-70%, which is in the range of optimized speckle size for 2D DIC (see [20]).

The dynamic test has been performed in a different test stand (Fig. 2c), where the available space for the camera was narrower, therefore an IDS 5490SE-M-GL camera was used. The IDS camera resolution is

3264x2448 px, the working distance was about 300 mm and the obtained resolution, with the selected 6 mm focal length optics, was about 0.05 mm/px.

3. RESULTS OF EXPERIMENTAL TESTS ON PRE-STRESSED CONCRETE SLEEPERS

3.1. Results of the static test

Considering the case of the static test, the very first visible crack was recorded, by VT, at 62.9 kN (Fig. 4a, crack " α "). As expected, the crack appeared in the central region of the sleeper, where the maximum tensile stress was present. Increasing the load, the sleeper began to show multiple cracks at 72.9 kN, while such cracks tended to reach the neutral axis of the sleeper at 97.9 kN (Fig. 4b, cracks " α ", " α_i " and " α_{ii} ", the latter outside the speckled region). The test ended at 122 kN, when the sleeper failed completely.

Figure 4a highlights that small cracks can be hardly detected by VT, while, by 2D DIC, the detection of the crack proved to be significantly more accurate (Fig. 4c and d). Indeed, at each increment of load, a picture of the speckled area was taken by the camera and used to define the local strain field by correlation to the reference picture taken at 0 kN load level. Image processing was carried with the software VIC 2D by Correlated Solutions. Figures 4c and d show some examples of 2D DIC results, in terms of the maximum principal strain, for cracks α and α_i at about the same load levels of Figures 4a and b. It should be noted that the strain values reported in the figures are not representative of real strains (since along the crack the concrete obviously shows a discontinuity), but should be considered as "apparent strain" due to the output of the numerical differentiation used in 2D DIC computation to estimate the strain field from the displacement one. Nevertheless, the very large apparent strain values allow detecting the crack path even in the case of extremely small crack opening (Fig. 4c). This allows the early detection of cracks, when the opening is of the order of a few micrometres, i.e. well before it is visible by VT.

Regarding AE, a first approximation discussion is rightly given, while a more advanced and refined analysis will be given in Section 4. As expected, by increasing the load, the activity increased, as the amplitude and the energy of the hits did: Figures 5a and b exemplify such an activity in terms of, respectively, amplitude and cumulated energy for channel 1, located at one of the ends of the sleeper. As can be seen, the observed trend of AE activity was found to be coherent with the damage phenomenon:

according to the expected Kaiser effect [21], AE events were mainly generated during load increments, while they significantly diminished during load plateaus. Moreover, Figures 5c and d exemplify the same AE activity, but recorded by channel 6 located closer to the region of interest of the sleeper. From this point of view, it is worth noting the position of the sensors does not seem to be crucial: indeed, no significant differences could be highlighted between the amplitudes and the cumulated energy recorded by the six channels during the static test. This can be motivated remarking that (Fig. 3a):

1. the region of interest is located at the mid-span of the sleeper;
2. the sensors are organized in a symmetrical way with respect to the region of interest;
3. the distance between the sensors located at the ends and those located on the lateral sides was not so pronounced to highlight a significant influence on the structural attenuation of sound beams in the monitored material.

Finally, each AE channel recorded about 16000 AE events during the whole static test.

3.2. Results of the dynamic test

Considering the case of the dynamic test, just one crack initiated during the block load characterized by a maximum load level of 308 kN and it propagated till the total failure of the sleeper at the block load characterized by a maximum load level of 448 kN (Fig. 6a, crack " α "). As expected, the crack appeared in the central region of the rail seat, where the maximum tensile stress was present.

Figure 6b shows the development of crack α in terms of maximum principal apparent strain as monitored by 2D DIC at different fatigue load levels. A significant difference can be immediately highlighted with respect to the results observed during the static test: at its initiation, the shape and size of the crack are already very similar to the final ones. This can be only interpreted assuming multiple cracks initiate simultaneously in the tensile fatigue loaded part of the weakest section of the sleeper and, with the increment of the maximum load level and of the number of fatigue cycles, they propagate and coalesce to form the final crack. This interpretation is aligned to the literature [7] regarding brittle materials. The proposed rationale is also supported by the observed entity of the maximum principal apparent strain (Fig. 6b): at the initiation of the crack, the strain is very low because a large part of the damaged section is still

characterized by intact ligaments, which do not allow for large displacements between the faces of the multiple (small) cracks. On the other hand, close to the end of the test, the small cracks have coalesced in a smaller number of large cracks, the number of intact ligaments is drastically decreased and a larger opening of the loaded damaged section becomes possible allowing the onset of larger strains.

Concerning AE results, increasing the maximum fatigue load level, AE activity increased, again. In particular, Figures 7a and c show, as examples, the AE events recorded by channel 1 (located at the end of the sleeper close to the tested rail seat) and by channel 2 (located at the farthest end of the sleeper with respect to the tested rail seat), respectively. The Kaiser effect could be observed again, as well: a larger amount of AE events, characterized by higher amplitudes, occurred at the beginning of each fatigue block, when the new maximum fatigue load level was reached for the first time. Nevertheless, during the following fatigue block load cycles, the reduction of AE activity was generally and definitely less pronounced than in the case of the static test, likely due to the continuous cyclic driving force acting on the material and on the initiated cracks. Another important difference was observed with respect to the static test: channels 1 and 2 provided results qualitatively very similar to each other, but both lower amplitudes and one order of magnitude lower cumulated energy (Fig. 7b and d) characterized the latter. It is worth adding that, instead, no significant differences were highlighted between channel 1 and channels from 3 to 6 because all of them were located relatively close to the region of interest, i.e. within a maximum distance equal to 450 mm. On the other hand, channel 2 was located at about 2 m from the region of interest and the results clearly showed that such a distance is long enough to make significant the influence of both the geometrical (beam spreading) and the structural (interaction with the inherent granular and aggregated nature of the material) attenuations on the sound beam. Finally, each AE channel recorded about 516000 AE events during the whole dynamic test.

4. ADVANCED ANALYSIS OF ACOUSTIC EMISSION DATA

The AE results shown up to now refer to the total amount of recorded data: it is reasonable to expect such data are not just directly related to primary emissions (damage phenomena), but also to different types of secondary emissions (noise and interference), such as electro-magnetic noise, the action of servo-hydraulic

actuators, friction at constraints, etc. A second critical point of AE monitoring is the typical amount of recorded data, which, even considering short campaigns, can easily sum up to millions of events. These two inherent characteristics directly put AE monitoring and analysis into the field of Big Data Analytics [22]. From this point of view, many approaches are available in the literature ([23]-[24]) for post-processing AE events in concrete structures, but it is worth remarking most of them address the classification of fracturing modes, while, here, the need is to classify and discriminate what is meaningful for monitoring damage in sleepers and what is not. Nevertheless, such post-processing approaches range from rather simple graphical methods to very complex and sophisticated artificial intelligence algorithms, so the reader is referred to the specific literature for details ([13]-[14], [25]). It remains some of these approaches were applied to the present data: for the sake of brevity, just the most performant and successful approach is described and discussed in the following. In particular, it consists in a “pattern recognition” [26] tool, implemented within the Matlab® environment and to be applied to the recorded AE waveforms, based on “data clustering” [27] and on “unsupervised artificial neural networks” [28].

Before describing the algorithm and its results, it is worth remarking that, as for any pattern recognition activity, the first step is to understand and to define what has to be recognized within a data set. In the present case, concrete is a granular and aggregated material characterized by brittle failure: the energy released during fracturing is mainly related to the detachment of grain boundaries without the onset of plastic phenomena or of sliding between crystallographic planes. Such detachments happen suddenly emitting acoustic events with a peculiar morphology: the so-called “burst” ([13], Fig. 8a), i.e. a fast oscillating ramp to a maximum value followed by a slow oscillating decay in time. This morphology is very similar to a damped sinusoidal curve. In the present research, bursts are, then, the main target of the pattern recognition approach because their origin can be reasonably ascribed to the initiation and development of service damage in pre-stressed concrete sleepers.

4.1. Selection of the classifying features for pattern recognition

Chosen the target waveform for the analysis, the right choice of the signal features, allowing discriminating the different waveforms composing the analysed data set, is the next critical step. In the case of AE, the

most widely used classifying features are standardized ([29], Fig. 8a): number of hits, counts, amplitude, duration, rise time and energy. Other features can be added considering both the time and the frequency domains of AE signals: RMS, peak frequency, frequency centroid, etc. It is worth remarking the best set of classifying features depends on the peculiarities of the application at hand and should be optimized based on the application itself.

From this point of view, a qualitative, powerful and widespread evaluation tool is the “parallel coordinates” plot [30]. Figure 8b shows, as an example, the parallel coordinates plot applied to the AE hits recorded by channel 1 during the static test: data were enlisted and four groups were defined according to the magnitude of the amplitude of the analysed signals (0%-25%, 26%-50%, 51%-75% and 76%-100%). Finally, amplitude, energy, rise time, duration, RMS and counts were compared and evaluated in order to choose the best set of classifying features. The amplitude was chosen as the “driving” feature according to the aforementioned rationale according to which bursts, typically, present higher amplitude with respect to other secondary acoustic emissions. Nevertheless, as can be seen, a clear distinction of the groups is not preserved for energy, rise time, duration, RMS and counts, since a hazy dispersion is obtained in the case of each of them. This means that, for the present case, the only effective feature for applying pattern recognition, among the considered ones, should be the amplitude. On the other hand, synthesizing a whole waveform by just one of its features is not a robust approach because large uncertainties might be introduced in the classification, producing relevant quantities of either false positives or false negatives.

In order to solve the just described feature selection problem, a novel “Var*” classifying feature is here introduced. The rationale of this feature is based on the need to describe synthetically the typical morphology of a burst (Fig. 8a). In particular, any kind of AE event is characterized by an oscillating nature with several peaks reached during the time history of the signal. The typical peaks of a burst are characterized by a large variability of amplitude values, ranging from the level of the detection threshold to the absolute maximum one, while other kinds of waveforms usually show a more restrained statistical dispersion (variance) of such peaks. The formal definition of the Var* feature takes advantage of these observations as follows. Let be \bar{x} the set of all the sampled points of an AE signal in the time domain:

$$\bar{x}(t) = [x_1(t), x_2(t), \dots, x_n(t)] \quad (1)$$

and \bar{x}_{norm} its normalization with respect to the maximum amplitude value of the AE signal:

$$\bar{x}_{norm} = \frac{\bar{x}}{\max_{x_i \in \bar{x}}(\bar{x})} \quad (2)$$

Let also be Th_{norm} the normalized detection threshold with respect to the same maximum amplitude value:

$$Th_{norm} = \frac{Th}{\max_{x_i \in \bar{x}}(\bar{x})} \quad (3)$$

Then, the subset \overline{Pk}_{norm} of all the peaks of \bar{x}_{norm} higher than the normalized detection threshold is extracted:

$$\overline{Pk}_{norm} = \left\{ \bar{x}_{norm,i} \in \bar{x}_{norm} : \left. \frac{\partial \bar{x}_{norm}}{\partial t} \right|_{\bar{x}_{norm}=0} \wedge \bar{x}_{norm,i} \geq Th_{norm} \right\} \quad (3)$$

and its statistical variance is calculated:

$$\sigma_{norm}^2 = Var(\overline{Pk}_{norm}) \quad (4)$$

Finally, the Var^* feature is obtained as the de-normalization of the variance of the peaks with respect to the maximum amplitude value of the AE signal:

$$Var^* = \sigma_{norm}^2 \cdot \max_{x_i \in \bar{x}}(\bar{x}) \quad (5)$$

Figure 8b shows, along with the other features, the application of Var^* to the parallel coordinates analysis. As can be seen, the Var^* feature was able to preserve the distinction of the groups, as amplitude had done. This means amplitude and Var^* might be adopted, for the analysis at hand, as an effective set of

classifying features. In particular, the former represents the typical high amplitude levels of bursts, while the latter their inherent rise time and decay time.

It is worth adding the drawn conclusion, on the best set of classifying features, proved to be generally true for all the AE channels adopted during both the static and the dynamic tests.

4.2. Pattern recognition and data clustering

Pattern recognition and data clustering were applied by the so-called K-SOM algorithm, since it has already been successfully exploited in many classification researches on AE signals ([31]-[32]). Such an algorithm combines a “Self-Organizing Map” (SOM) [33] with a “k-Means” process [34]. The main flowchart of the applied approach is reported in Figure 8c, where the analysis of AE hits recorded by channel 1, during both the static and the dynamic tests, is shown as an example.

First, AE hits and the selected classifying features are given, as input, to the SOM, which is a common paradigm of artificial neural network with an unsupervised batch training process, used to define a map of the similarities between the analysed signals. The choice of an unsupervised approach, for the analysis of AE signals, is suggested in the literature [25] on the rationale according to which no information on the nature of the expected hits is usually available in advance. The SOM was implemented into the Matlab® environment and was characterized by a plane architecture subdivided into a hexagonal lattice, while its topological function was exploited by a Gauss function [33]. The output of SOM consists of the so-called “Unified Distance Matrix” (U-matrix), which is a strained grid of neurons where their distance represents the similarity between the analysed signals (Fig. 8c). The size of the map was defined by means of the heuristic formula $N = M^{0.543}$, where N is the number of adopted neurons and M is the size of the analysed set of signals. From this point of view, to avoid over classification, the number of neurons was limited to a grid of maximum size equal to 30x20 ([31]-[32]). It is worth adding that, up to this point, a severe reduction of significant patterns was obtained, since the number of neurons was, typically, several orders of magnitude lower than that of the original input set of signals.

The U-matrix is, then, passed to the k-Means algorithm, which is an iterative partitional algorithm, adopting square-error minimization, and used to divide the signals, based on the similarities reported into

the U-matrix itself, in a predetermined number of clusters. Since the optimized number of clusters cannot be known *a priori*, several automatic tools are available in the literature. Anyway, the heuristic approach [35] is the most common on purpose and, then, it is the one exploited in this research. Figure 8c shows the result of the pattern recognition algorithm, which resulted to be optimized adopting 4 clusters. The same optimized number of clusters was observed from the analysis of all the other AE channels recorded during both the tests.

4.3. Numerical validation of the developed pattern recognition algorithm

A pattern recognition process is influenced by several acting factors introducing uncertainties and, consequently, false positive and false negative results. Examples of such factors are the adopted algorithm, the size of the whole data set to be analysed, the chosen classifying features and their dispersion among each single signal composing the data set. An investigation about the robustness and the sensitivity of the proposed procedure is, then, mandatory and two dedicated numerical experiments were defined and applied on purpose. It is worth noting that the dissertation on both numerical experiments requires an anticipation of the classification results, which, on the other hand, will be presented and discussed in detail in Section 4.4.

The first numerical experiment consisted in a sensitivity analysis in terms of the minimum level of signal to noise ratio (SNR) which guarantees to classify a burst as such. In particular, the steps of the analysis were as follows:

1. a pilot noise signal (an example is given in Figure 9a) and a pilot burst signal are randomly extracted from the entire set of experimentally acquired AE events;
2. the amplitudes of the pilot burst are scaled so that the maximum one is equal to the maximum amplitude of the pilot noise (an example is given in Figure 9b);
3. a controlled set of artificial, i.e. numerically defined, AE signals is built summing the pilot noise, whose amplitude is always the same, to different variations of the scaled pilot burst obtained multiplying its amplitudes by a SNR factor K ranging from 0.5 to 5 with a step equal to 0.1. Figures 9c

and d show the examples of the artificial signals defined for the cases of K equal to 0.7 and 2, respectively;

4. the controlled set of artificial signals is introduced into the entire set of experimentally acquired AE events and the proposed pattern recognition algorithm is applied;
5. the minimum K value for which the artificial signals are classified into the cluster(s) of bursts is searched for and annotated;
6. steps from 1 to 5 are repeated one hundred times.

Eventually, it was found that the average value of the K factor, leading to the correct classification of the pilot bursts, corresponded to $K = 2$, which is the typical SNR value for all the technical applications where signals are influenced by the background noise. This allows concluding that the sensitivity of the proposed pattern recognition algorithm is within more than reasonable levels.

The second numerical experiment was carried out to assess the robustness of the proposed pattern recognition algorithm, i.e. the number of generated false positive and false negative results. The steps of the analysis were as follows:

1. 450 experimental waveforms are randomly extracted from the entire set of experimentally acquired AE events: 50 of them, representing the whole range of observed amplitudes, from the cluster(s) of bursts and 400 from the cluster(s) of noise;
2. for each of the 50 bursts, the frequency spectrum is extracted and used to define, by means of slight random variations of spectral amplitudes, 10 artificial bursts;
3. for each of the 400 noisy signals, the frequency spectrum is extracted and used to define, by means of slight random variations of spectral amplitudes, 100 artificial noisy signals;
4. a controlled set of artificial AE signals is, then, built summing up all the 40500 artificial signals. The chosen proportion of bursts and noisy signals resembles the experimental one, according to which bursts are approximately 1%-2% of the whole set.
5. the controlled set of artificial signals is analysed by the proposed pattern recognition algorithm;
6. classification results are evaluated by defining two concise parameters: i) the ratio A between the bursts classified into the cluster of bursts with respect the overall number of bursts; ii) the ratio B

between the number of bursts classified into the cluster of bursts with respect to the total waveforms inserted in such cluster;

7. steps from 1 to 6 are repeated one hundred times.

Eventually, the average values of parameters A and B resulted to be 74% and 81%, respectively.

Considering parameter A, the meaning of the found value is that 26% of the bursts were classified in clusters mainly related to noise. In the amplitude vs. Var* plane, all the misclassified bursts were found to be close to the boundary between the cluster of bursts and the adjacent ones, suggesting the existence of a region of uncertainty where the classification process fails due to the relevant similarity between bursts and noise in terms of the chosen classifying features. Nevertheless, the misclassified bursts were those characterised by the lowest values of the classifying features, which could be associated to the less relevant damage development. The complementary 74% artificial bursts, which were related to the most significant damage information, were classified in the right way.

On the contrary, considering parameter B, the meaning of the found value is that 19% of the signals (a value comparable to that highlighted by parameter A) was classified in the cluster of bursts, but it was, actually, noise. As for the case of parameter A, the misclassified signals were located, in the amplitude vs. Var* plane, around the boundary between the cluster of bursts and the adjacent ones, revealing the region of uncertainty acts both ways, i.e. both burst classified as noise and noise classified as burst. Nevertheless, the misclassified noisy signals represented, again, the less relevant AE events in the cluster of bursts and their contribution, in terms of energy erroneously attributed to damage development, could be considered negligible.

This allows concluding, again, that the performance of the proposed pattern recognition algorithm is within more than reasonable levels.

4.4. Results and discussion

A summary of the results obtained by the analysis of AE signals recorded during the static and the dynamic tests is reported in Figures 10 and 11, respectively, while the following sections provide a discussion.

4.4.1. Static test

Figure 10a shows, as an example and in terms of amplitude vs. time, the classification results for channel 1: on 15993 AE events, 98% were included in cluster #1, 1.78% in cluster #2, 0.2% in cluster #3 and 0.02% in cluster #4. This could have been anticipated, qualitatively, analysing the topology of the U-matrix (Fig. 8c): just one cluster, i.e. #1, included both the largest portion of neurons and all the AE events recorded during the application of the load levels lower than 62.9 kN, at which the very first visible crack was observed. This seems to suggest such a cluster might represent noise, while the others (#2, #3 and #4) should include bursts due to damaging, as well.

The Var* vs. amplitude plot (Fig. 10b) is also informative because it allows understanding how the magnitude and dispersion of the values of the classifying features played a role in the clustering process. It is worth highlighting that a linear correlation between amplitude and Var* clearly exists and that clusters #2, #3 and #4 are distributed in regions where the amplitude and Var* features are characterized by significantly higher magnitudes than cluster #1.

In order to deepen the nature of the signals included into each cluster, an investigation of the waveforms was, then, carried out. Figure 10c shows some examples: as can be seen, cluster #1 presents waveforms morphologically very different with respect to a burst, confirming the hypothesis it is the “noise cluster”. Since it includes 98% of all the acquired signals, it can be concluded most of the experimental effort (number of acquisitions, data storage, post-processing computational time, etc.) was spent on useless data. Actually, this was due to the choice, described in Section 2.3, to avoid the application of any filtering on acquisitions, in order to get the highest flexibility during the post-processing and the analysis of the phenomenon. On the other hand, a preliminary definition and optimization of acquisition criteria, in order to decrease the amount of useless data during on-site monitoring, has been assessed elsewhere already [36].

Clusters #2, #3 and #4 mainly include burst signals (Fig. 10c) and, consequently, they should have defined just one cluster all together. In the case of cluster #4, the definition of a dedicated cluster can be easily explained noting that all of its signals are distorted, from the point of view of the pattern recognition algorithm, by saturated amplitudes, i.e. amplitude levels larger than the full-scale acquisition value of the

adopted equipment. The subdivision of the other bursts into clusters #2 and #3 reflects, instead, the fact that they have a very wide range of the amplitude and Var* features. An optimization of the post-processing procedure in order to avoid the distribution of similar signals into different clusters is an open point of this research.

Finally, Figure 12a shows the trend, of clusters #2 and #3 summed together, of the cumulated energy recorded by channel 1. As can be seen comparing the data to 2D DIC monitoring, the steepest increments of energy are immediately followed by either the initiation or a significant propagation of cracks, confirming again the importance of detecting and analysing bursts for the application at hand.

All the outcomes, described and highlighted in the present Section for channel 1, were found to be similar for all the other channels, as well.

4.4.2. Dynamic test

As for the static test, Figure 11a shows, in terms of amplitude vs. time, the classification results for channel 1: on 515920 AE events, 42% were included in cluster #1, 32% in cluster #2, 24% in cluster #3 and 2% in cluster #4. Such figures and the analysis of the topology of the U-matrix (Fig. 8c) highlight relevant differences with respect to the static test: the size of clusters #1, #2 and #3 is comparable, while cluster #4 is significantly smaller. On the other hand, the latter includes the signals characterized by the highest amplitudes (Fig. 11a), likely the AE bursts searched for. It is also worth noting the highest recorded amplitudes are lower than those observed during the static test, even if channel 1, during the dynamic one, was significantly closer to the location of the AE source (Fig. 3a and b): it seems that fatigue damaging of concrete is more silent than the quasi-static one. Finally, in the case of the dynamic test, the trend of the highest amplitudes increases roughly linearly over time, while, in the case of the static test, it keeps roughly constant after the initiation of cracks. This seems to be an evidence of the progressive and continuous development of damage micro-sites in fatigued concrete with respect to the instantaneous and discrete damage macro-ones observed under quasi-static load conditions.

The Var* vs. amplitude plot (Fig. 11b) confirms a linear correlation, between amplitude and Var*, in the case of fatigue damaging, as well. Moreover, the signals included in cluster #4 are distributed in a region

where the amplitude and Var* features are characterized by significantly higher magnitudes than clusters #1, #2 and #3.

In order to get more insight and confirm the first impressions, the nature of the signals included in the four clusters was investigated, again, by checking (Fig. 11c) the morphology of the waveforms belonging to each of them. Contrarily to the static test, where the clusters gathering bursts were more than one, here the classification led to the definition of just one group of bursts (#4) that, for all the channels, corresponded to the one having the smallest size. The other three clusters (#1, #2 and #3) gathered many other morphologies of signal, mainly not related to bursts and to the damage of the sleeper. This can be ascribed to the fact that, in this case, bursts showed a dispersion of the amplitude and Var* features significantly lower than in the case of the static test.

Finally, Figure 12b shows the trend of the cumulated energy of the signals recorded by channel 1 and included in cluster #4. As for the case of the static test, the comparison of such a trend to 2D DIC monitoring shows that the steepest increments of energy are related to relevant developments of the damage.

All the outcomes, described and highlighted in the present Section for channel 1, were found to be similar for all the other channels, as well.

5. DAMAGE LOCALIZATION BY ACOUSTIC EMISSION

One of the advantages of SHM by AE consists in the possibility to localize sources of AE events [13]. In particular, knowing the sound speed in the monitored material (see Section 2.3 for the considered concrete), the arrival times of the signals, acquired by a suitable network of coordinated sensors, can be properly treated, by rather simple mathematical models, to estimate the position of such sources in the monitored structure. Summarizing [13], the minimum number of sensors for a “1D localization” in 1D structures is 2, for a “2D localization” in 2D structures is 3 and for a “3D localization” in 3D structures is 4.

Railway sleepers can be schematised as 1D beams, so a 1D localization was applied in the present research. In this case, the mathematical expression for calculating the position L of the AE source along the line linking the two sensors is [14]:

$$L = \frac{v \cdot (t_1 - t_2) + s}{2} \quad (6)$$

where v is the sound speed into the material, t_1 and t_2 are the times flight taken by a given AE hit to reach the two sensors and s is the linear distance between the two sensors themselves. As anticipated in Section 2.3, the localization process was activated (Fig. 3a and b) between sensors 1 and 2 located at the ends and for each pair of sensors (3 and 4, 5 and 6) located close to the region of interest and lying on the same lateral side of the tested sleeper. For the sake of brevity, just the results obtained by the sensors located at the ends are here described, because they realize the most compact and affordable set-up for on-site monitoring of sleepers and because the other pairs, from the point of view of localization, did not add any new useful information.

Figure 13a shows, in terms of cumulated energy vs. the position of the correspondent sources, all the AE events localized during the static test and compares them to the real position of the monitored cracks (α , α_i and α_{ii}): it is rather difficult to separate the signals related to the developing damages and those related to other secondary noisy sources. The same conclusion could be drawn observing the same diagram, compared to the real position of the monitored crack (α), for the case of the dynamic test (Fig. 13c).

The previously described outcomes of the proposed pattern recognition algorithm, which allows to consider just the signals related to damage, came straight at hand for a more detailed and accurate analysis of localization results. Figures 13b and d show the same diagrams of Figures 13a and c, but based on the acquired bursts only. First, it is evident that, in agreement with the results of the pattern recognition process, the number of relevant data is definitely lower than the total number of signals. Actually, it has to be added that not all the burst signals, highlighted by the pattern recognition algorithm applied to the acquisitions of each single channel, provided a useful result from the point of view of localization. This is a well-known issue of the localization procedure of AE events [13]: indeed, during real-time monitoring, some events can be missed by at least one sensor of the 1D network, leading to an inapplicability of Eq. (6) and the consequent loss of localization data. On the other hand, it remains that a better and easier interpretation of localization results is evident, because, during both the tests, most of the energy related

to classified and localized bursts is centred on the region where the cracks actually initiated and propagated. The observed dispersion of the results can be ascribed to different factors. The first one is the value of the estimated sound speed in the material: indeed, the value reported in Section 2.3 (3320 m/s) was derived as the average of the experimental values acquired from eight different sleepers and was adopted as a reference for all the sleepers tested here. Another factor influencing the dispersion of localization results is the assumption of the 1D scheme: actually, this is an approximation because, in general, the localized events do not lay exactly on the line connecting the sensors, but are scattered in the sections of the sleeper around such a line. Then, the application of Eq. (6) to a “slight” 2D or 3D configuration introduces approximation and uncertainties whose level is related to how far the monitored structure is from the assumed 1D mathematical model. Nevertheless, it is worth concluding that, from the point of view of a practical on-site application of AE localization to sleepers, the suggestions given by Figures 13b and d can be still considered meaningful and reasonable.

Finally, it is worth noting that the 1D localization procedure, based on placing the sensors at the ends of the sleeper, was able to provide meaningful information about the damaging phenomena occurring at both the mid-span (static test) and the rail seat (dynamic test) regions. In particular, the latter, although not symmetrical and likely penalized by the larger distance of channel 2 from the AE source, still resulted able to provide useful information. This allows concluding that just two sensors, placed at the ends of the sleeper, provide the total coverage for the monitoring of the sleeper itself and the localization of AE sources. If localization were not requested, just one sensor, located at one of the ends, could provide an effective monitoring performance, simplifying the set-up and decreasing the total cost of the SHM of sleepers.

6. CONCLUDING REMARKS

In order to guarantee rail operation safety, the integrity of sleepers is fundamental, therefore International Standards impose strict test to be carried out on finished products for homologation. During these tests, a key parameter is the early detection and the measurement of the evolution of cracks in the concrete. Visual inspections are usually applied for crack detection and monitoring, both with microscopes and digital

cameras. Acquired images can be analyzed manually or by automatic digital image processing techniques, however only cracks on the surface of the sleeper can be detected. In this paper, the applicability of the acoustic emission technique for early detection of cracks has been proposed and validated against the vision-based approach. The advantage of the proposed approach is that AE can detect also cracks inside the sleepers. The technique has been validated both in static and dynamics tests on sleepers, demonstrating the reliability of the technique. As expected, in all the tests AE detected an increase of the activity and of the energy, while the applied load increases. Moreover, the AE activity was found to be coherent with the damage phenomenon.

An advanced analysis of AE data, based on artificial intelligence pattern recognition techniques, has been proposed in the work, in order to recognize, amongst the huge amount of acquired events, only the ones due to primary emissions, which are linked to mechanical damage of the sleepers.

Finally, the position of the cracks has been estimated by means of AE data analysis, demonstrating that, in concrete sleepers, a successful 1D localization of the crack position can be obtained. If localization is not needed, just one sensor located at one of the two ends of the sleeper could provide an effective and affordable monitoring performance.

This paper is an extended version of the first part of the research work presented [37] at the International Symposium on Structural Health Monitoring and Nondestructive Testing held at Saarbrücken (Germany) in 2018. In the mentioned paper, a preliminary and low-cost version of the methodology proposed herein has been developed and validated, as well, but this second part is now being deepened and will be published in a future paper.

ACKNOWLEDGMENTS

The Authors would like to thank Ms. Rosa Piazzolla, Mr. Fabio Valla and Mr. Rui Liu for the active help given to the research. PoliINDT (Inter-Department Lab for Structural Diagnostics and Monitoring) at Politecnico di Milano is also acknowledged for its technical support in carrying out acoustic emission measurements.

REFERENCES

- [1] C. Esveld, *Modern railway track*, II Ed., MRT Productions, Zaltbommel, (2016) 241.
- [2] International Union of Railways, SuWoS, UIC report 2013.
- [3] K. Navaratnarajah, B. Indraratna, Application of under sleeper pads to enhance the sleeper-ballast interface behaviours, *Proc. Indian Geotechnical Conference (IGC-2018)*, Bengaluru, India, 2018.
- [4] C. Gonzalez-Nicieza, M.I.A. Ivarez-Fernandez, A. Menendez-Diaz, A.E. Ivarez-Vigil, F. Ariznavarreta-Fernandez, Failure analysis of concrete sleepers in heavy haul railway tracks, *Engineering Failure Analysis* 15 (2008) 90–117.
- [5] W. Ferdous, A. Manalo, Failures of mainline railway sleepers and suggested remedies –Review of current practice, *Eng. Fail. Anal.*, 44 (2014) 17–35.
- [6] S. Kaewunruen, A.M. Remennikov, Progressive failure of prestressed concrete sleepers under multiple high-intensity impact loads, *Eng. Struct.*, 31 (2009) 2460-2473.
- [7] D. Munz, T. Fett, *Ceramics – Mechanical Properties, Failure Behaviour, Materials Selection*, Springer Verlag, 1999.
- [8] Railway applications-track-concrete sleepers and bearers - Part 2: pre-stressed monoblock sleepers, European Standard, EN 13230-2.
- [9] E. Resendiz, L.F. Molina, J.M. Hart, J.R. Edwards, S.V. Sawadisavi, N. Ahuja, C.P.L. Barkan, Development of A Machine Vision System for Inspection of Railway Track Components, *Proc. 12th World Conference on Transport Research*, Lisbon, Portugal, 2010.
- [10] S. Minoura, T. Watanabe, M. Sogabe, K. Goto, Analytical Study on Loading Capacity of Prestressed Concrete Sleeper, *Procedia Engineering* 199 (2017) 2482–2487.
- [11] A. F. Jr. Grandt, *Fundamentals of structural integrity*, John Wiley & Sons Inc., Hoboken, USA, 2003.
- [12] C. Boller, Ways and options for aircraft structural health management, *Smart Mater Struct* 10 (2001) 432–440.
- [13] M. Ohtsu, *Acoustic Emission and Related Non-destructive Evaluation Techniques in the Fracture Mechanics of Concrete*, Woodhead Publishing Series, 2015.
- [14] C. U. Grosse, M. Ohtsu, *Acoustic Emission Testing*, Springer-Verlag, 2008.

- [15] M.A. Sutton, J.J. Orteu, H.W. Schreier, *Image Correlation for Shape, Motion and Deformation Measurements*, Springer Science+Business Media, 2009.
- [16] M. Di Benedetti, S. Cholostiakow, H. Fergani, E. Zappa, A. Cigada, M. Guadagnini, *3D-DIC for strain measurement in small scale GFRP RC specimens*, SMAR 2015 – Third Conference on Smart Monitoring, Assessment and Rehabilitation of Civil Structures, Antalya, Turkey, 2015.
- [17] S. Cholostiakow, M. Di Benedetti, M. Guadagnini, C+. Gowda, J. Barros, E. Zappa, *Experimental and numerical study on the shear behaviour of geometrically similar FRP RC beams*, 8th International Conference on Fiber Reinforced Polymer (FRP) Composites in Civil Engineering (CICE2016), Hong Kong, China, 2016.
- [18] RFI TCAR SF AR 03 002 F, *Concrete Sleepers RFI 230, RFI 240 and RFI 260 – Technical Specification for Provision*, RFI, 2017. [In Italian]
- [19] N.N. Hsu, F.R. Breckenridge F.R., *Characterization and Calibration of Acoustic Emission Sensors*, *Materials Evaluation* 39 (1981) 60-68.
- [20] C. Lane, R. Burguete, A. Shterenlikht, *An objective criterion for the selection of an optimum DIC pattern and subset size*, *Society for Experimental Mechanics - 11th International Congress and Exhibition on Experimental and Applied Mechanics 2008*, vol. 2, pp. 900–908, 2008.
- [21] C. Li, E. Nordlund, *Experimental verification of the Kaiser effect in rocks*, *Rock Mech. Rock Engng.* 26 (1993) 333-351.
- [22] A. Deshpande, M. Kumar, *Artificial Intelligence for Big Data*, Packt Publishing, 2018.
- [23] M.A.A. Aldahdooh, N.M. Bunnori, *Crack classification in reinforced concrete beams with varying thicknesses by mean of acoustic emission signal features*, *Const. Build. Mat.*, 45 (2013) 282–288.
- [24] A. Farhidzadeh, A.C. Mpalaskas, T.E. Matikas, H. Farhidzadeh, D.G. Aggelis, *Fracture mode identification in cementitious materials using supervised pattern recognition of acoustic emission features*, *Const. Build. Mat.*, 67 (2014) 129–138.
- [25] ASNT, *Nondestructive Testing Handbook Vol. 6: Acoustic Emission Testing*, 3rd edition, American Society for Nondestructive Testing, Inc., 2005.
- [26] C.M. Bishop, *Pattern Recognition and Machine Learning*, Springer Verlag, 2006.

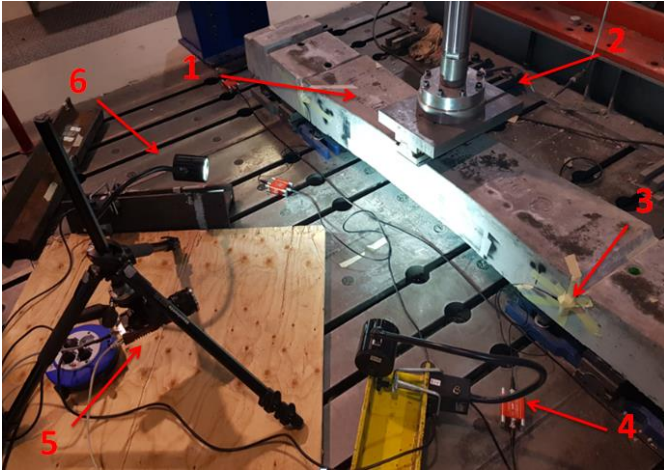
- [27] C.C. Aggarwal, C.K. Reddy, Data Clustering: Algorithms and Applications, Chapman and Hall/CRC, 2013.
- [28] S. Haykin, Neural Networks and Learning Machines, 3rd edition, Pearson College Div., 2008.
- [29] Non-destructive testing -- Acoustic emission inspection – Vocabulary, International Standard, ISO 12716.
- [30] A. Inselberg, Parallel Coordinates, Springer Nature Switzerland AG, 2009.
- [31] D. Crivelli, M. Guagliano, A. Monici, Development of an artificial neural network processing technique for the analysis of damage evolution in pultruded composites with acoustic emission, Composites: Part B 56, (2014) 948–959.
- [32] J.P. McCrory, S.K. Al-Jumaili, D. Crivelli, M.R. Pearson, M.J. Eaton, C.A. Featherston, M. Guagliano, K.M. Holford, R. Pullin, Damage classification in carbon fibre composites using acoustic emission: A comparison of three techniques, Composites: Part B, 68 (2015) 424–430.
- [33] J. Vesanto, E. Alhoniemi, Clustering of the self-organizing map, IEEE Trans Neural Netw, 11 (2000) 586–600.
- [34] S. Günter, H. Bunke, Validation indices for graph clustering, Pattern Recogn Lett, 24 (2003) 1107–13.
- [35] A.K. Jain, Data clustering: 50 years beyond k-means, Pattern recognition letters, 31 (2010) 651–666.
- [36] R. Piazzolla, F. Valla, An Acoustic Emission-based Approach to Structural Health Monitoring of Railway Pre-stressed Concrete Sleepers, MSc Thesis, Politecnico di Milano, 2018.
- [37] M. Carboni, A. Collina, R. Liu, E. Zappa, A preliminary feasibility analysis about the structural health monitoring of railway concrete sleepers by acoustic emission and digital image correlation, International Symposium on Structural Health Monitoring and Nondestructive Testing, Saarbrücken, Germany, 2018.

List of Figures

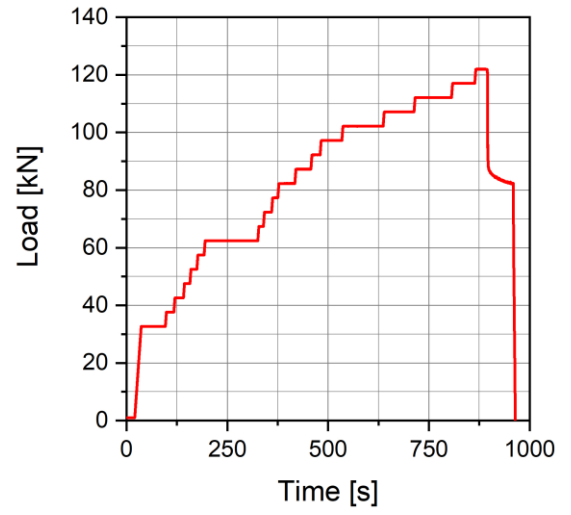
- Figure 1 – Examples of railway prestressed concrete sleepers.
- Figure 2 – Experimental tests on sleepers: a) experimental set-up for the static test (1 - sleeper, 2 - actuator, 3 - piezoelectric sensors, 4 - preamplifiers, 5 - digital camera, 6 - lights); b) applied static load-time history; c) experimental set-up for the dynamic test; d) applied dynamic load-time history.
- Figure 3 – Set-ups for structural health monitoring and non-destructive testing (dimensions in [mm]): a) static test; b) dynamic test; c) example of speckled region of interest for 2D DIC (static test).
- Figure 4 – Experimental results of the static test: a) very first visible crack “ α ” (62.9 kN); b) multiple cracks “ α ”, “ α_I ” and “ α_{II} ”, the latter outside the speckled region (97.9 kN); c) 2D DIC maximum principal strain of crack “ α ” (72 kN); d) 2D DIC maximum principal strain of cracks “ α ” and “ α_I ” (97 kN).
- Figure 5 – Acoustic emission activity recorded by channel 1 and channel 6 during the static test: a) and c) amplitude of AE events and load history vs. time; b) and d) cumulated energy of AE events and load vs. time.
- Figure 6 – Experimental results of the dynamic test: a) fatigue crack “ α ” (448 kN); b) 2D DIC maximum principal strain due to crack “ α ” at different values of the applied maximum fatigue load level.
- Figure 7 – Acoustic emission activity recorded by channel 1 and channel 2 during the dynamic test: a) and c) amplitude of AE events and maximum fatigue load vs. time; b) and d) cumulated energy of AE events and maximum fatigue load vs. time.
- Figure 8 – Pattern recognition and clustering of AE data: a) scheme of an AE burst; b) example of parallel coordinates plot (static test, channel 1); c) clustering flowchart (static and dynamic tests, channel 1).
- Figure 9 – Numerical validation of the developed pattern recognition algorithm.
- Figure 10 – Results of the pattern recognition process applied to the AE hits recorded during the static test (channel 1): a) classification in terms of amplitude; b) Var* vs. amplitude plot; c) relevant example of hits included into the defined clusters.
- Figure 11 – Results of the pattern recognition process applied to the AE hits recorded during the dynamic test (channel 1): a) classification in terms of amplitude; b) Var* vs. amplitude plot; c) relevant example of hits included into the defined clusters.
- Figure 12 – Comparison between the trend of the cumulated energy and the outcomes of the 2D DIC monitoring: a) static test (channel 1); b) dynamic test (channel 1).
- Figure 13 – Results of the localization process in terms of cumulated energy vs. AE source position (1D localization by sensors 1 and 2): a) static test, all signals; b) static test, just bursts; c) dynamic test, all signals; d) dynamic test, just bursts.



Fig. 1



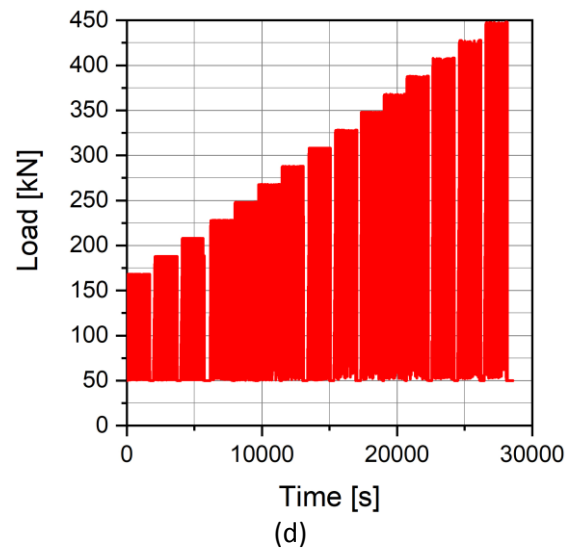
(a)



(b)

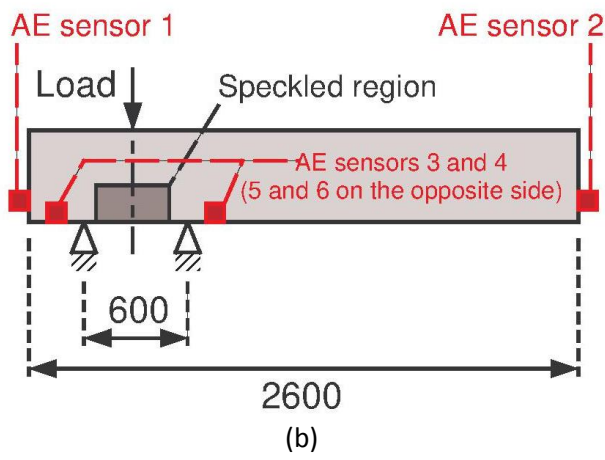
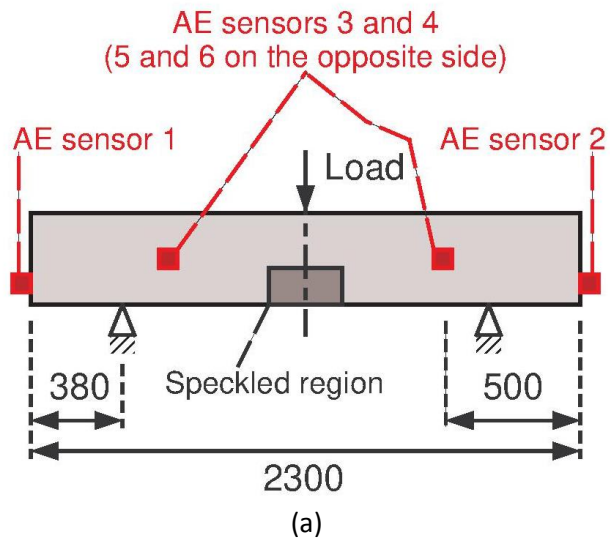


(c)



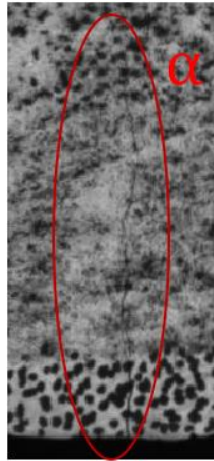
(d)

Fig. 2

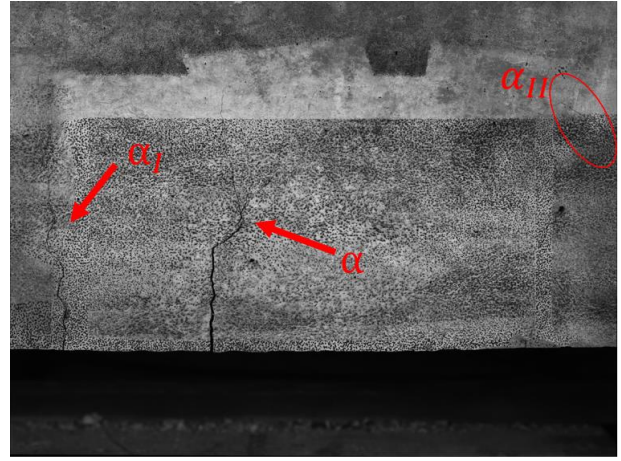


(c)

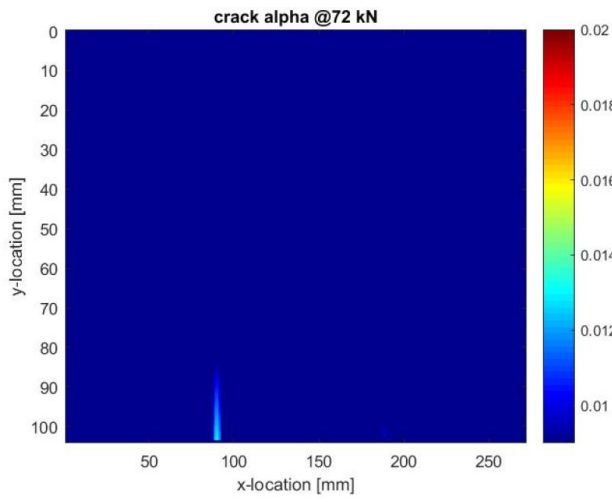
Fig. 3



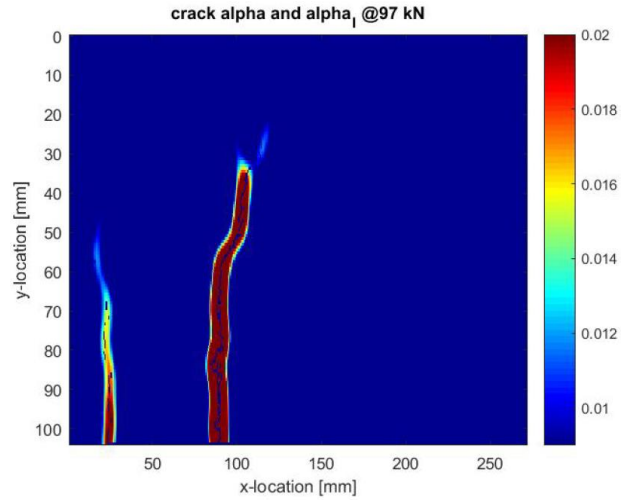
(a)



(b)



(c)



(d)

Fig. 4

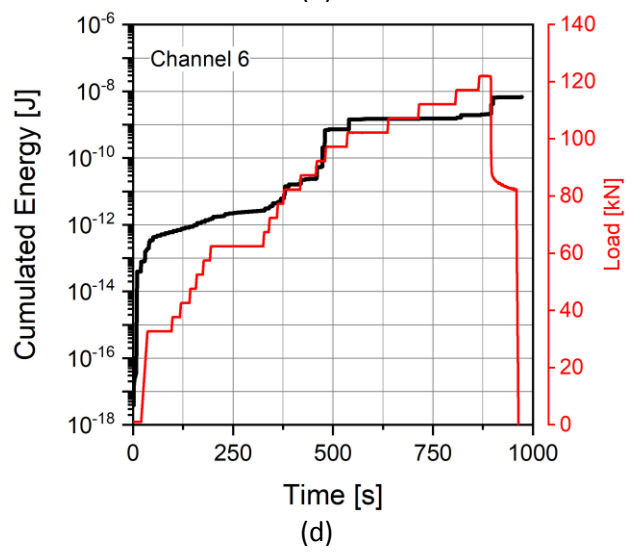
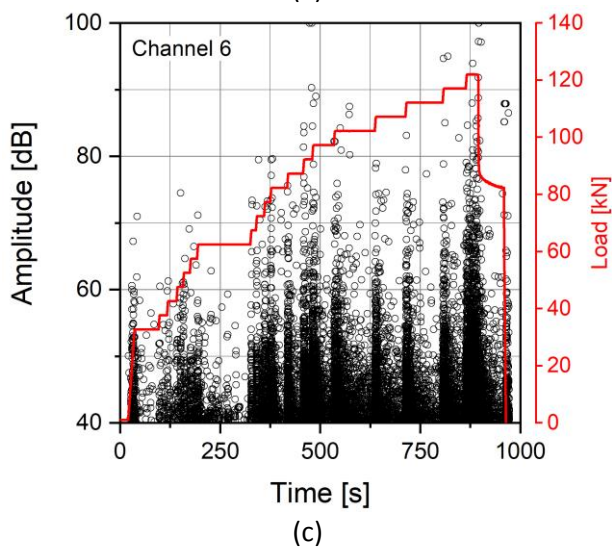
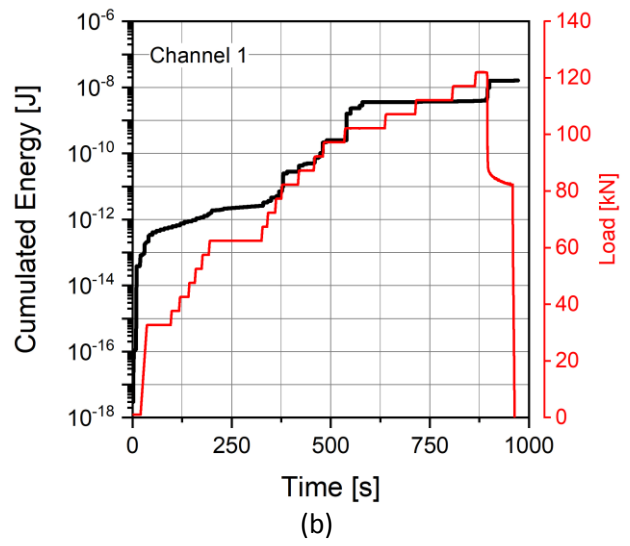
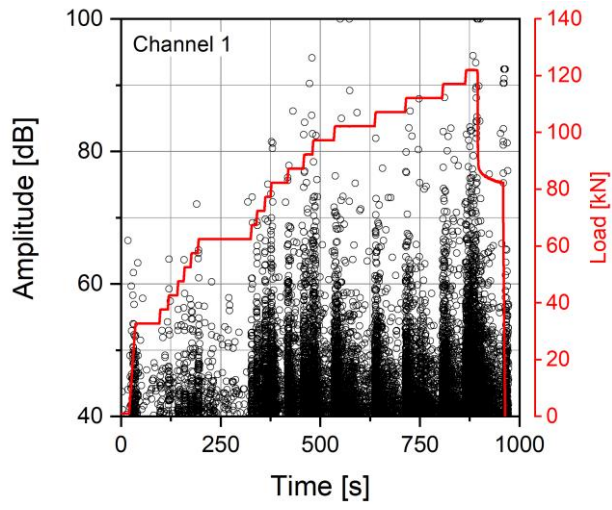
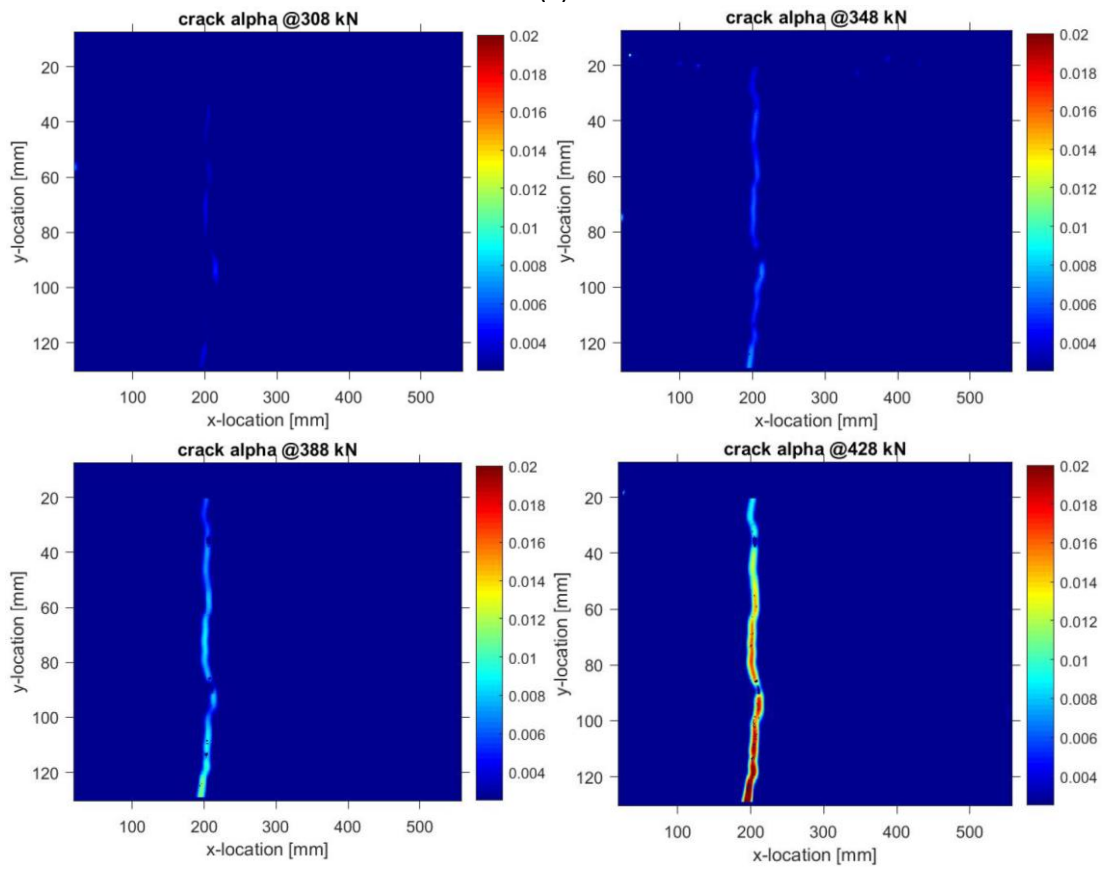


Fig. 5

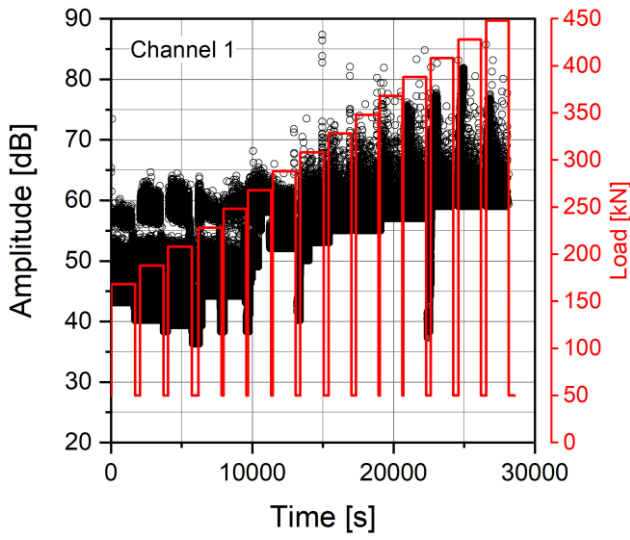


(a)

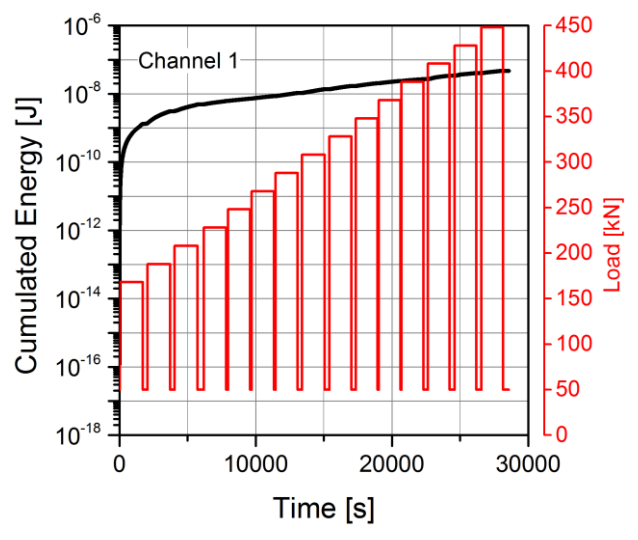


(b)

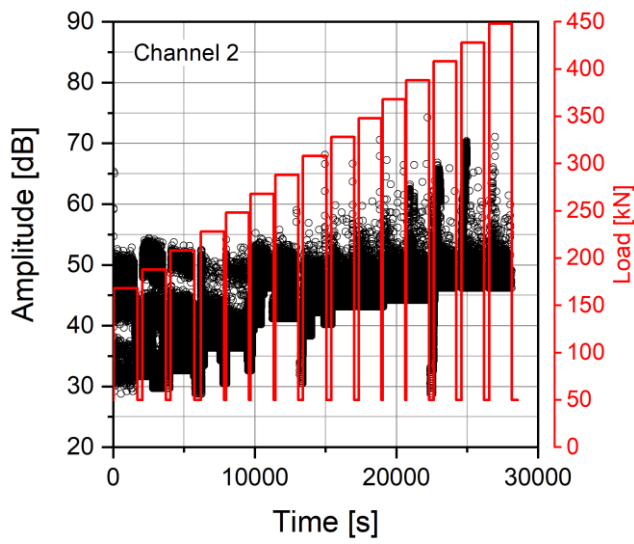
Fig. 6



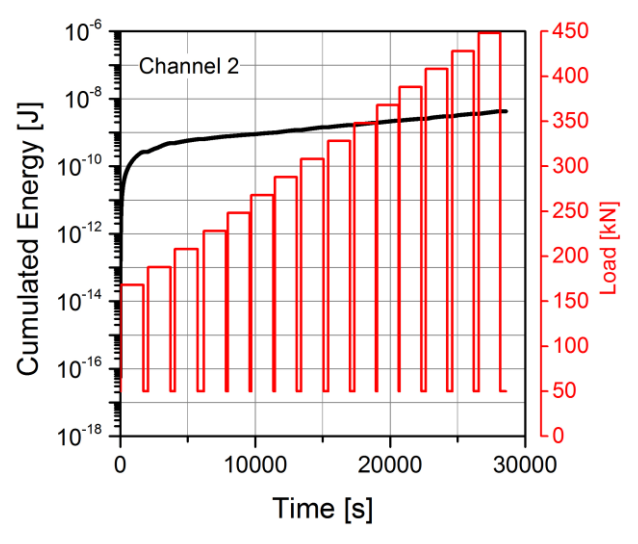
(a)



(b)

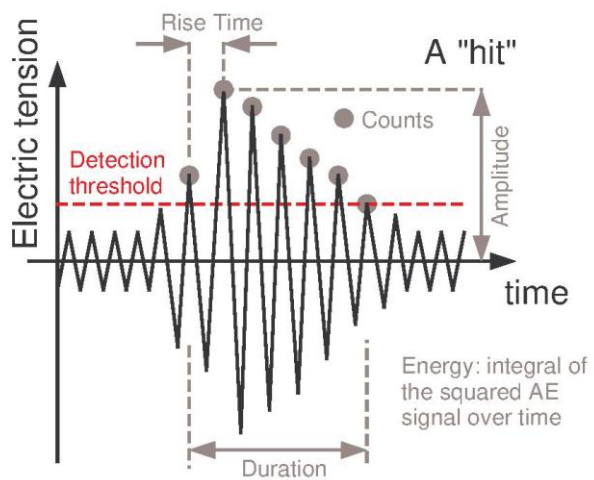


(c)

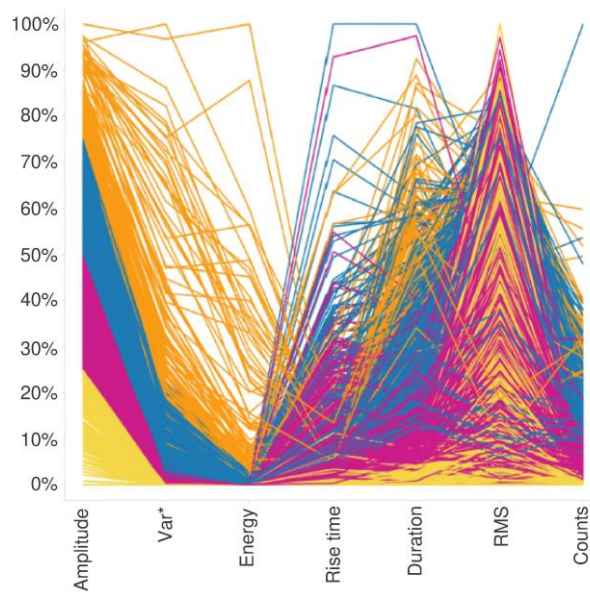


(d)

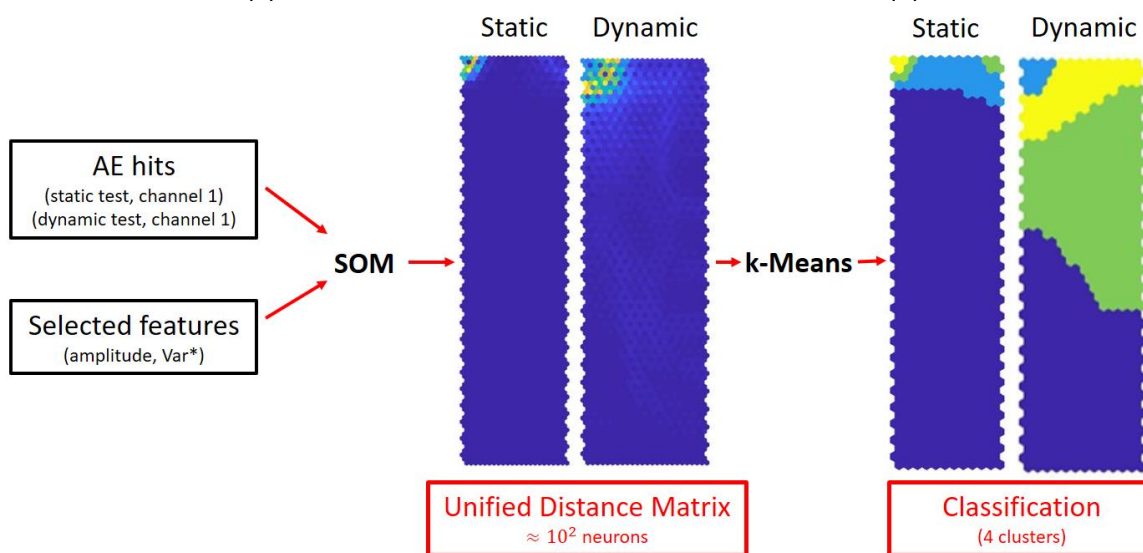
Fig. 7



(a)

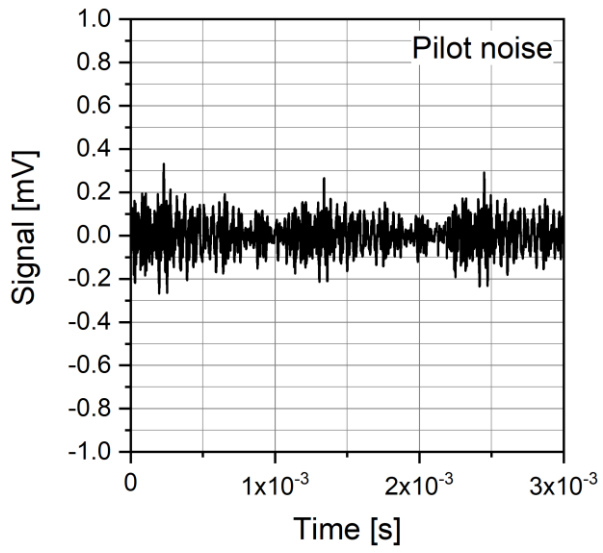


(b)

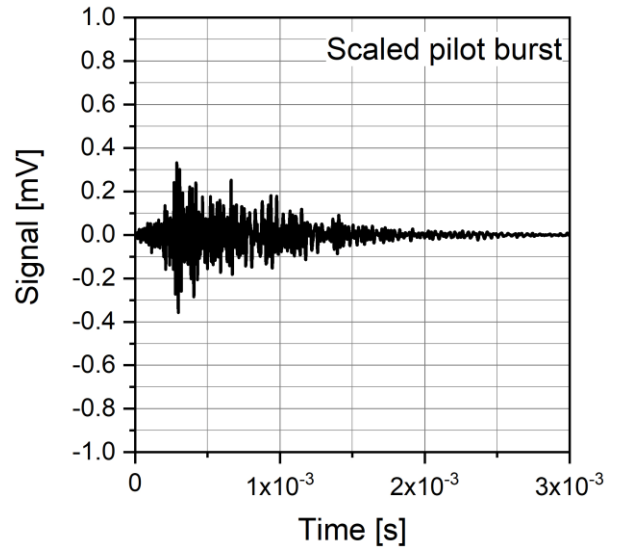


(c)

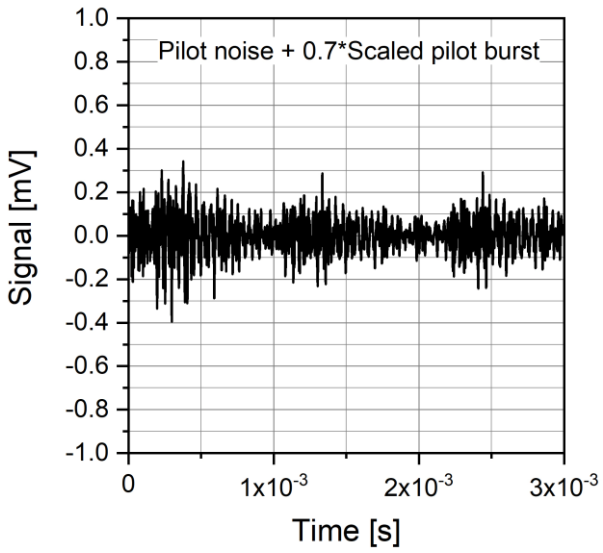
Fig. 8



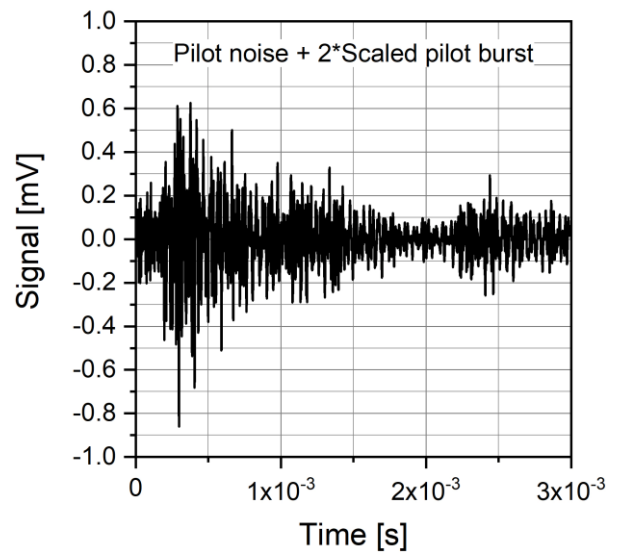
(a)



(b)



(c)



(d)

Fig. 9

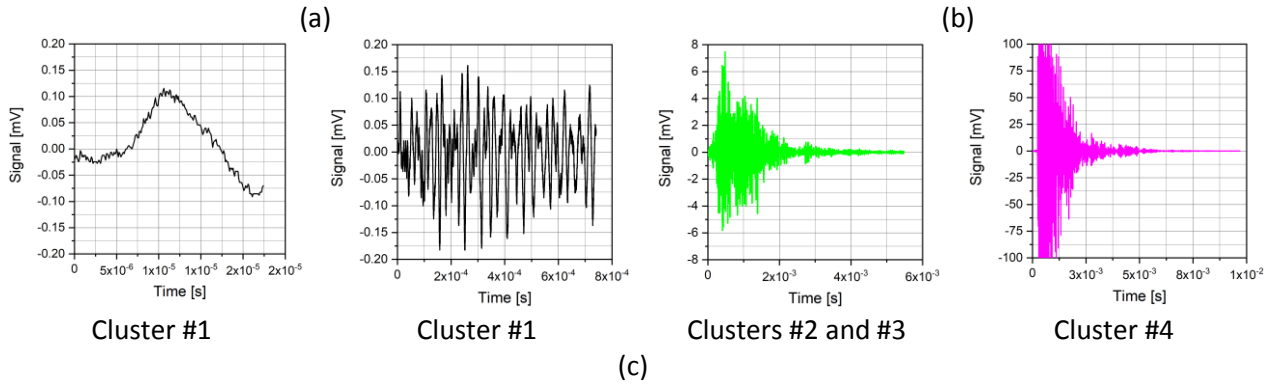
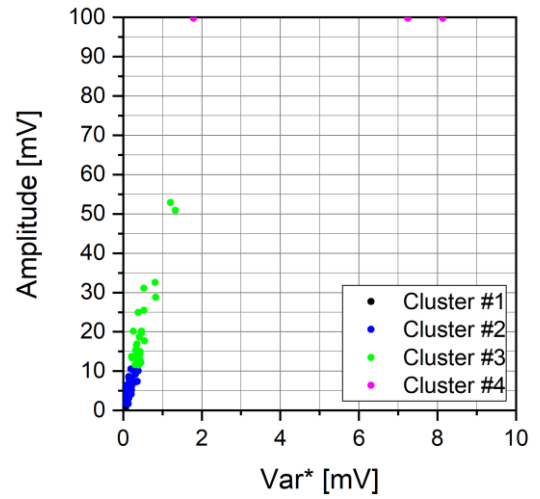
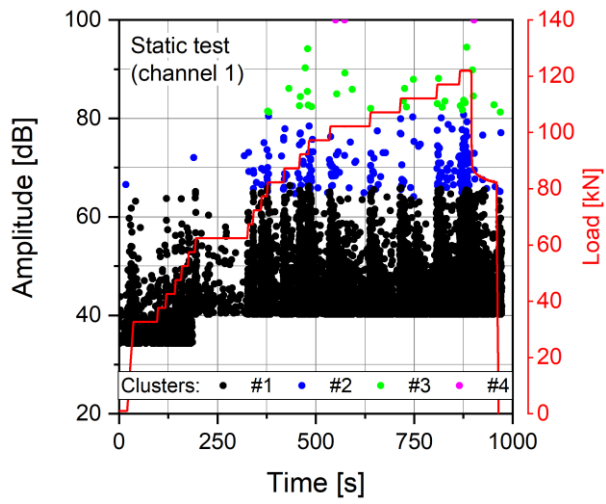
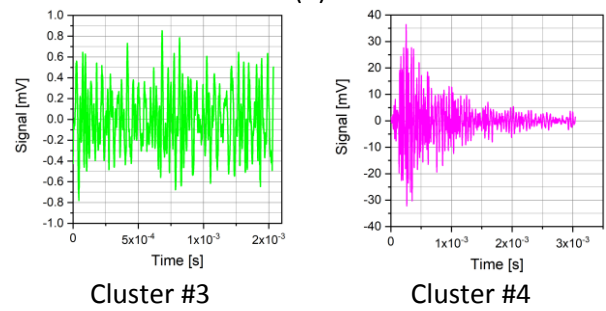
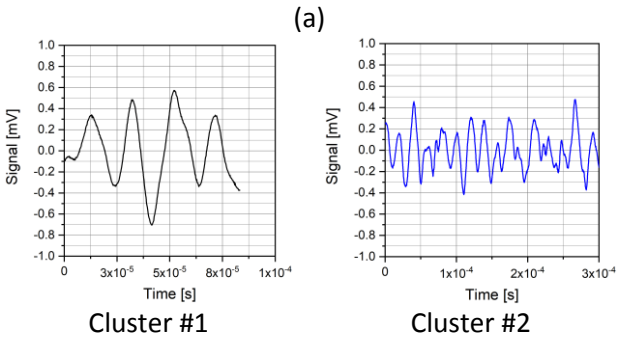
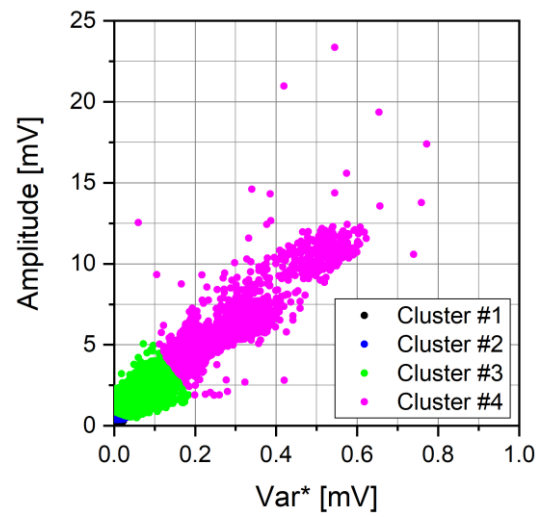
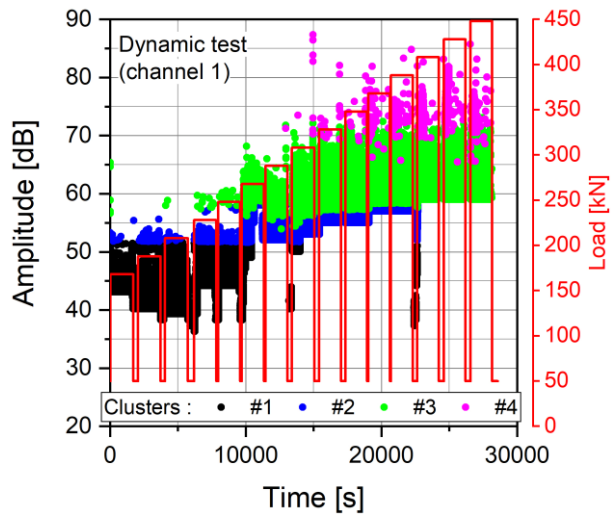
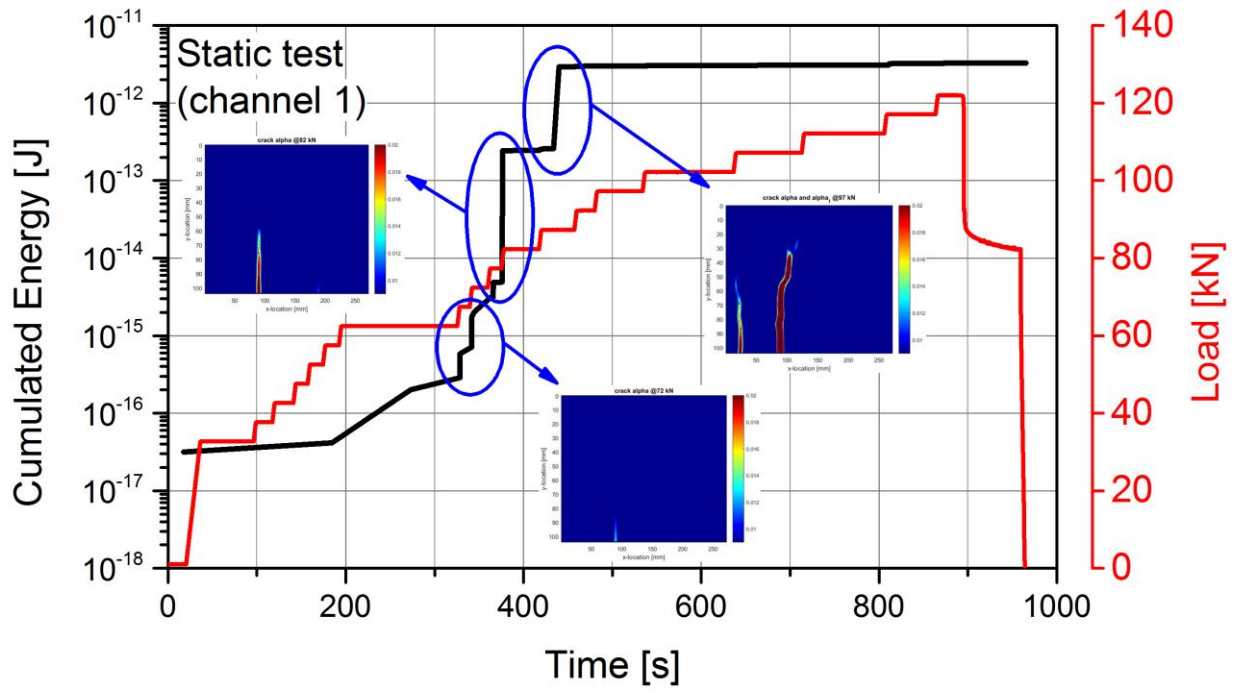


Fig. 10

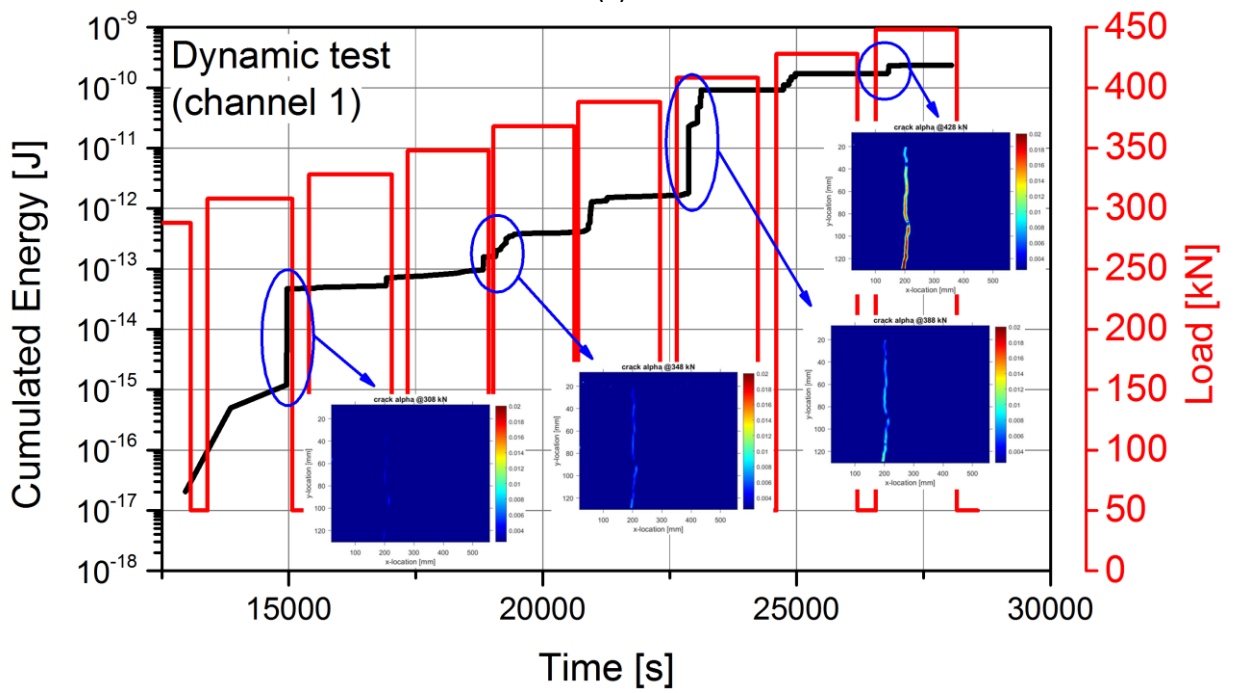


(c)

Fig. 11



(a)



(b)

Fig. 12

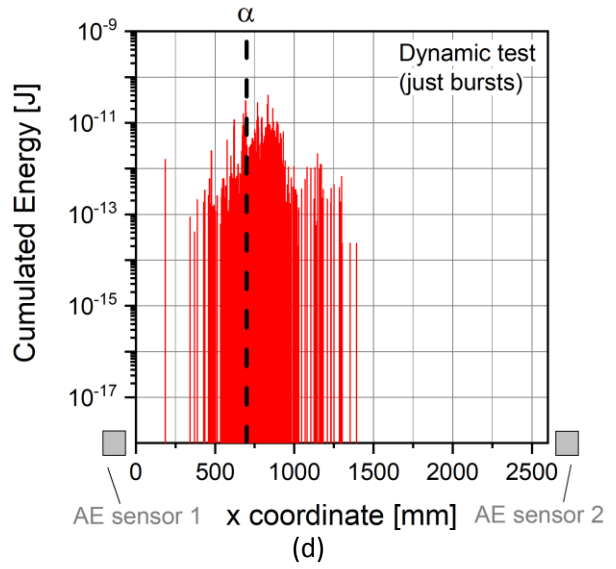
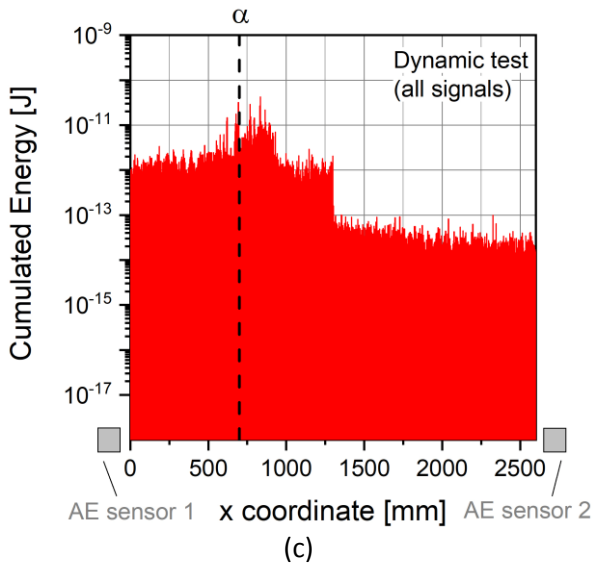
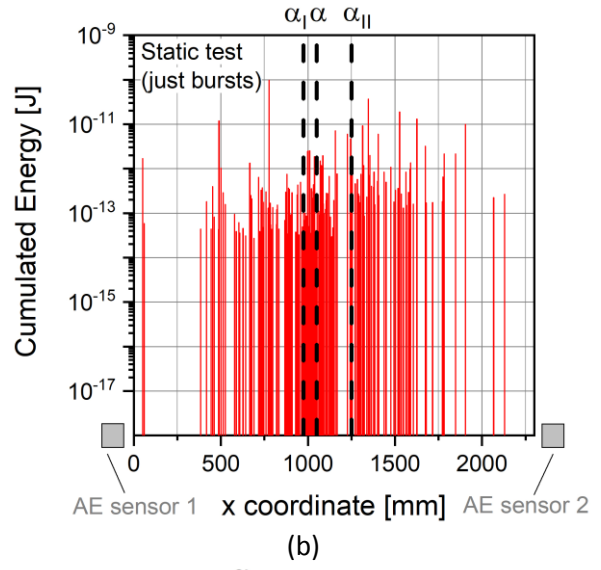
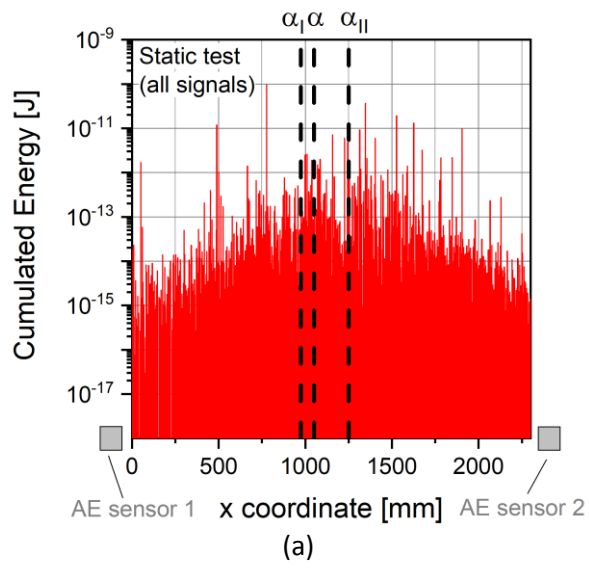


Fig. 13